Nonlinear sensitivity enhancement of resonant microsensors and its application to low power magnetic sensing

2011 J. Micromech. Microeng. 21 045004

(http://iopscience.iop.org/0960-1317/21/4/045004)

J. Micromech. Microeng. **21** (2011) 045004 (12pp) doi:10.1088/0960-1317/21/4/045004

Nonlinear sensitivity enhancement of resonant microsensors and its application to low power magnetic sensing

Seungkeun Choi, Yong-Kyu Yoon[1], Seong-Hyok Kim and Mark G Allen

School of Electrical and Computer Engineering, Georgia Institute of Technology, 777 Atlantic Drive NW, Atlanta, GA 30332, USA

E-mail: seungkeun.choi@gatech.edu and mallen@gatech.edu

Received 14 November 2010, in final form 21 January 2011
Published 25 February 2011
Online at stacks.iop.org/JMM/21/045004

Abstract

Nonlinearities in resonating structures can be used to increase the sensitivity of sensors based on these structures. An example system, a torsional resonant magnetic sensor, is analyzed to illustrate the effect. The system is composed of a disk-type silicon resonator combined with a permanent magnet supported by multiple micromachined silicon beams, excitation and sensing coils, and a magnetic feedback loop. The effects of nonlinearity on sensitivity have been characterized as a function of beam width and the number of beams using analytical models as well as numerical analysis. By increasing the number of beams while reducing the beam width (and thereby maintaining constant nominal linear resonant frequency), large nonlinearity has been obtained, resulting in an increased change in operating resonant frequency per unit applied magnetic field. The interaction between an external magnetic field surrounding the sensor and the permanent magnet generates a rotating torque on the silicon resonator disk, changing the effective stiffness of the beams and therefore the resonant frequency of the sensor. By monitoring shifts in the resonant frequency while changing the orientation of the sensor with respect to the external magnetic field, the direction of the external magnetic field can be determined. Self-resonance-based electromagnetic excitation of the mechanical resonator enables it to operate with very low power consumption and low excitation voltage. A total system power consumption of less than 140 μW and a resonator actuation voltage of 1.4 mVrms from a $\pm$1.2 V power supply have been demonstrated with a sensitivity of 0.28 Hz/rotational degree to the Earth's magnetic field.

(Some figures in this article are in colour only in the electronic version)

1. Introduction

MEMS-based mechanically resonant sensors, in which the sensor resonant frequency shifts in response to the measurand, are widely utilized [5]. Resonant sensors with frequency output are of particular interest, as frequency can be measured with high precision. Such sensors are typically operated in their linear resonant regime. However, substantial improvements in the resonant sensors' performance (functionally defined as the change in resonant frequency per unit measurand change) can be obtained by designing the sensors to operate far into their nonlinear regime [10, 18, 20]. Significant efforts have been focused on understanding the nonlinearity associated with the large oscillation amplitude of resonators, and tuning it externally [18, 20]. For example, Kozinsky *et al* use a nonlinear model with a third-order Taylor series expansion of the electrostatic forcing applied to a nanoresonator in order to tune the effective Duffing coefficient using an external electrostatic potential. They are able to tune nonlinearity and, consequently, the dynamic range and resonant frequency of nanomechanical resonators [20]. However, less attention has been given to how nonlinearity can be increased by changing the resonator geometry, and how to

[1] Present address: Department of Electrical and Computer Engineering, University of Florida, 217 Benton Hall, Gainesville, FL 32611.

exploit the increasing nonlinearity to increase the sensitivity of resonant sensors.

As an example, consider a magnetic field sensor for detecting the Earth's magnetic field. Such an electronic compass system is finding applications in ultra-low-power mobile devices, such as wristwatches, smart phones, and portable global positioning systems (GPS). Hence, developing a small-size, low-power-consumption, and low-operation-voltage magnetic field sensor that can detect the direction of the Earth's magnetic field is of great interest.

Even though there have been a variety of approaches to the electronic compass successfully demonstrated [8, 23, 24], such as Hall-effect sensors [27, 31, 32, 39], fluxgate [2–4, 11, 13, 16, 25, 26, 28, 29, 33–35], anisotropic magnetoresistance (AMR) sensors [30, 31, 36, 37, 40], giant magnetoresistance sensors [31, 36, 37], resonant magnetic sensors [1, 5–7, 12, 15, 19, 21, 38], and magnetometers [17, 41], the realization of extremely low power electronic compasses has been elusive.

Earlier, we reported an electrostatically excited, epoxy-based micromachined resonant magnetic field sensor that exhibited very low power consumption with sensitivity sufficient to measure the Earth's magnetic field [22]. A resonant comb drive structure was fabricated with a photo-definable epoxy (SU-8) and a permanent magnet (NdFeB) was glued onto the center of the comb drive disk. The interaction between an external magnetic field and the permanent magnet causes a shift in the fundamental resonant frequency (f_c) of the device. Although the operating voltage was lower (~10 V) compared to most of the other electrostatic-based sensors, the limited thermal and mechanical stabilities of SU-8 were drawbacks. Alternatively, we demonstrated a low-driving voltage (100 mV) and CMOS-compatible silicon-based resonant magnetic field sensor incorporating a permanent magnet, an external coil for the excitation, and an assembled Hall-effect sensor for the detection. However, it consumed significant power mainly due to the Hall-effect sensor [9].

This paper presents a complete magnetic sensing system that consumes less than 200 μW of power in continuous operation, and is capable of sensing the Earth's magnetic field. The system is composed of a micromachined silicon resonator combined with a permanent magnet, excitation and sensing coils, and a magnetic feedback loop for the completion of the system. This effect is illustrated through the use of a magnetically torqued, rotationally resonant MEMS platform. Platform structural parameters, such as the beam width and the number of beams, are parametrically varied subject to the constraint of constant small-deflection resonant frequency.

2. Device concept and theoretical modeling

Consider a permanent magnet torsionally supported on a resonant disk, which is in turn supported by flexures (figure 1). The interaction between an external magnetic field H such as the Earth's magnetic field and the magnetization of the permanent magnet M generates a torque that deflects and may change the stiffness of the beam, resulting in a change in the resonant frequency of the sensor (figure 1).

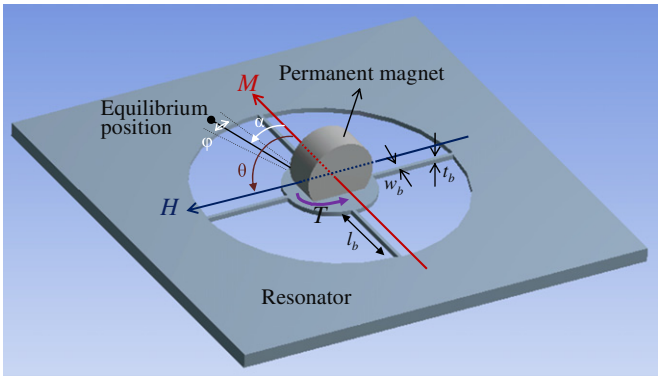

Figure 1. A silicon resonator structure with a permanent magnet. M is the magnetization direction of the magnet, H is the direction of the external magnetic field, α is the rotational angle of the permanent magnet, φ is the small oscillation angle at resonance, and θ is the angle between H and M. l_b, w_b, and t_b are the beam length, beam width, and beam thickness, respectively. Torque (T) is generated on the silicon resonator disk due to the interaction between M and H.

When the magnetization (M) and the external magnetic field (H) are not perfectly aligned (θ is neither 0° nor 180°), the center disk rotates by an angle α due to the magnetic torque (T) (figure 1) to reach the equilibrium position. This angle is determined by solving the equilibrium equation, stating that the torques acting on the system must sum to zero,

$$k_1\alpha - T_0 \sin(\theta - \alpha) = 0, \tag{1}$$

where k_1 is the torsional linear stiffness coefficient of the beams and T_0, the maximum amplitude of the magnetic torque, is given by equation (2) for a magnet of volume V and magnetization M.

$$T_0 = \mu_0 M V H, \tag{2}$$

where $\mu_0 = 4\pi \times 10^{-7}$ H m^{-1} is the permeability of free space. In the case of large rotation angles, the beams are subject to large deflections and their load-deflection behavior is no longer linear [14]. A cubic term multiplied by a torsional nonlinear stiffness coefficient, k_{nl}, has to be added to the equilibrium equation,

$$k_1\alpha + k_{nl}\alpha^3 - T_0 \sin(\theta - \alpha) = 0. \tag{3}$$

Nonlinear effects have to be taken into account whenever the deflection (approximated to the product of the angle of deflection, α, and the radius of the center disk, r) is comparable to or larger than the width of one beam, w_b [14]. The beams tend to stiffen as the angular deviation increases. Hence, the resonator oscillating around the new equilibrium position, α, exhibits a higher resonant frequency. Assuming a torsional vibratory system with a single degree of freedom, the expression for the fundamental resonant frequency of the sensor is obtained by solving the differential equation satisfied by the angle of oscillation, φ [22],

$$I\ddot{\varphi} + k_1(\alpha + \varphi) + k_{nl}(\alpha + \varphi)^3 = T_0 \sin(\theta - (\alpha + \varphi)), \tag{4}$$

where I is the platform moment of inertia of the system. For small oscillation angles of φ, equation (4) becomes

$$I\ddot{\varphi} + (k_1 + 3k_{nl}\alpha^2 + T_0\cos(\theta - \alpha))\varphi = T_0 \sin(\theta - \alpha) - k_1\alpha - k_{nl}\alpha^3. \tag{5}$$

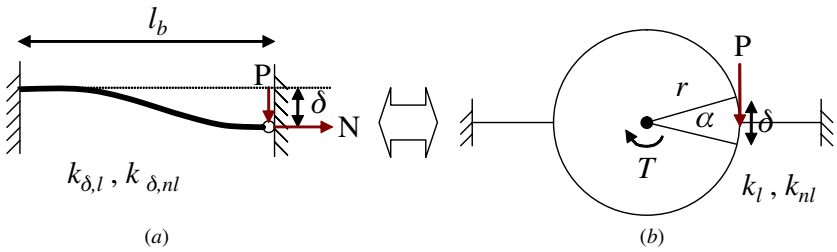

Figure 2. (*a*) Clamped-guided beam model to find lateral linear ($k_{\delta,1}$) and nonlinear ($k_{\delta,\mathrm{nl}}$) stiffness coefficients, and (*b*) disk-type resonator and torsional linear (k_1) and nonlinear (k_{nl}) stiffness coefficients.

Hence, when the magnetization and the external magnetic field are not perfectly aligned, the resonant frequency of the system is

$$f_c = \frac{1}{2\pi}\sqrt{\frac{k_1 + 3k_{\mathrm{nl}}\alpha^2 + T_0\cos(\theta-\alpha)}{I}}. \tag{6}$$

To solve this equation, k_1, k_{nl}, and the relationship between θ and α have to be determined. Figure 2 shows that k_1 and k_{nl} can be approximated by the nonlinear equations of the beam that has one end clamped and the other end guided subject to large deflection [14].

When the direction of magnetization is parallel to the external field, the magnetic torque is zero and the static resonator does not experience any rotation, i.e. $\alpha = 0$. However, when the resonator is oscillating, the torque increases as the rotational resonator is pulled away from its equilibrium position. Assuming small oscillation and negligible damping, equation (4) can now be expressed as

$$I\ddot{\varphi} + k_1\varphi - T_0\sin(\theta-\varphi) = 0. \tag{7}$$

Hence, when the direction of magnetization is parallel to the external field, the expression of the resonant frequency is given by

$$f_c = \frac{1}{2\pi}\sqrt{\frac{k_1 + T_0\cos\theta}{I}}, \tag{8}$$

where θ is 0° or 180°.

Numerical values of the torsional linear (k_1) and nonlinear (k_{nl}) stiffness coefficients are obtained by considering the torque and force relationship, as shown in figure 2,

$$T = k_1\alpha + k_{\mathrm{nl}}\alpha^3 = P\cdot r = k_{\delta,1}\cdot r\cdot\delta + k_{\delta,\mathrm{nl}}\cdot r\cdot\delta^3, \tag{9}$$

$$= k_{\delta,1}\cdot r^2\cdot\alpha + k_{\delta,\mathrm{nl}}\cdot r^4\cdot\alpha^3. \tag{10}$$

Therefore, the torsional linear (k_1) and nonlinear stiffness (k_{nl}) coefficients of the resonator with the number of beams (N_b) are

$$k_1 = N_b k_{\delta,1} r^2 \quad \text{and} \quad k_{\mathrm{nl}} = N_b k_{\delta,\mathrm{nl}} r^4. \tag{11}$$

The deflection δ for a concentrated load P at the end of a beam of length l_b, thickness t_b, mass moment of inertia I, and elastic modulus E where the loaded end of the beam is guided, as shown in figure 2(*a*), can be found by simultaneously solving the following equations [14],

$$P = \frac{E\cdot t_b\cdot w_b^4}{3\cdot l_b^3}\sqrt{\frac{2}{3}}u^3\left(\frac{3}{2} - \frac{1}{2}\tanh^2 u - \frac{3}{2}\frac{\tanh u}{u}\right)^{-\frac{1}{2}}, \tag{12}$$

$$\delta = w_b\sqrt{\frac{2}{3}}(u - \tanh u)\cdot\left(\frac{3}{2} - \frac{1}{2}\tanh^2 u - \frac{3}{2}\frac{\tanh u}{u}\right)^{-\frac{1}{2}}, \tag{13}$$

$$u = \sqrt{\frac{N}{EI}}\left(\frac{l_b}{2}\right), \tag{14}$$

where N is the normal force that develops in the beam as a result of the applied force. The numerical values for the applied force (P) and the deflection (δ) are calculated at a given u (12)–(14). As a result, the force (P) can be expressed as a function of the deflection (δ). The functional relationship between deflection and force is described using the following equation,

$$P = k_{\delta,1}\delta + k_{\delta,\mathrm{nl}}\delta^3, \tag{15}$$

where $k_{\delta,1}$ and $k_{\delta,\mathrm{nl}}$ are lateral linear and nonlinear stiffness coefficients of a single beam with one end clamped and one end guided, respectively. Equation (15) is further modified to find the stiffness coefficients easily as

$$\frac{P}{\delta} = k_{\delta,\mathrm{nl}}\delta^2 + k_{\delta,1}. \tag{16}$$

The theoretical analysis is performed on a silicon micromechanical resonator, which consists of a permanent magnet torsionally supported by four beams. The sensitivity of the resonator is characterized by varying the width of the beams (10, 20 and 30 μm). All other parameters are listed in table 1. A cylindrical permanent magnet is used throughout modeling and measurement (figure 1). Figure 3 shows plots from (16) where lateral linear ($k_{\delta,1}$) and nonlinear ($k_{\delta,\mathrm{nl}}$) stiffness coefficients are found. The nonlinear stiffness coefficient ($k_{\delta,\mathrm{nl}}$) is the slope of this curve and the linear stiffness coefficient ($k_{\delta,1}$) is the intercept of the curve with the y axis. The torsional stiffness of the beams, k_1 and k_{nl}, are calculated using (11). The inset in figure 3 shows the nonlinear deflection of a beam. T_0 are 7.6×10^{-8}, 1.5×10^{-6}, and 2.9×10^{-6} N m for the external magnetic fields 50 μT, 0.975 mT, and 1.95 mT, respectively.

Once k_1 and k_{nl} are found, the nonlinear equation (3) is solved numerically with MATLAB to find the deviation angle (α) as a function of θ. Finally, the resonant frequency is calculated using (6). Figures 4(*a*) and (*b*) show the plot of α (in degree) as a function of θ (in degree) and the resonant frequency of the magnetic field sensor as a function of θ for the beam width of 20 μm. As the external magnetic field

Table 1. Parameters used for theoretical analysis.

Young's modulus silicon (E_{si}) (GPa)	165	Young's modulus magnet (E_{magnet}) (GPa)	152
Density of silicon (kg m^{-3})	2330	Density of magnet (kg m^{-3})	7440
Beam thickness (t_b) (μm)	200	Magnet radius (r_m) (μm)	800
Beam width (w_b) (μm)	10, 20, 30	Magnet thickness (t_m) (μm)	800
Beam length (l_b) (mm)	2	Number of beams	4
Center disk radius (r_{si}) (mm)	1	Mass moment of inertia (kg m^2)	3.3 × 10^{-12}

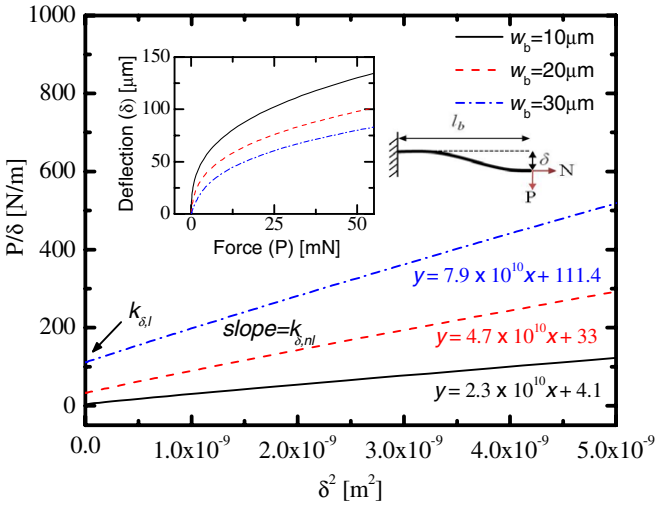

Figure 3. A nonlinear deflection of a single beam where one end is clamped and the other end is guided. The lateral nonlinear stiffness coefficient ($k_{\delta,nl}$) corresponds to the slope and the lateral linear stiffness coefficient ($k_{\delta,l}$) is found at the intercept $\delta^2 = 0$. The inset shows the nonlinear dependence of the deflection on the applied force.

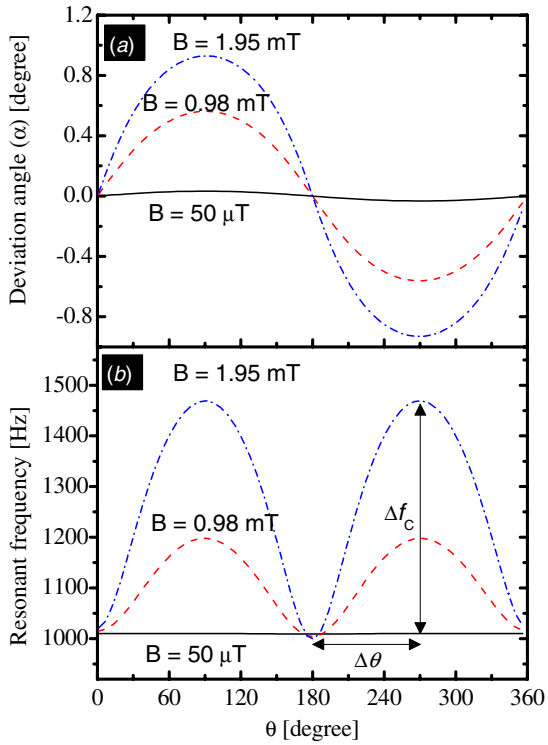

Figure 4. (*a*) Variation in the deviation angle (α) and (*b*) variation in the resonant frequency as a function of θ at the external magnetic fields of 50 μT, 0.975 mT, and 1.95 mT. The simulation model has four beams and a beam width of 20 μm. The difference between the maximum and minimum resonant frequencies divided by the minimum resonant frequency over $\theta = 0^\circ$ and 90° is taken as a measure of sensor performance.

increases, both the deviation angle and the resonant frequency increase at a given θ due to the increased rotational torque.

For resonators with three different beam widths, the numerical values of k_l and k_{nl} are listed in table 2 along with resonant frequencies and the normalized sensitivities calculated at external magnetic fields of 50 μT, 0.975 mT, and 1.95 mT. The normalized sensitivity is defined as the difference between the maximum resonant frequency (f_{max}) and minimum resonant frequency (f_{min}) divided by the minimum resonant frequency (f_{min}), as the resonator is rotated between $\theta = 0^\circ$ and 90°. The effect of increasing nonlinearity sensitivity can be argued from (6). Consider first the calculation of f_{min}. According to (8), the minimum resonant frequency (f_{min}) occurs at $\theta = 0^\circ$, where the torque T_0 is zero because the direction of magnetization is parallel to the external field. As T_0 increases from zero, both linear (k_l) and nonlinear (k_{nl}) terms of (6) additively increase the resonant frequency. Therefore, the normalized sensitivity, $(f_{max} - f_{min})/f_{min}$ per rotational degree, will be larger if the nonlinear terms are present. This will be developed more rigorously below.

2.1. Case 1: $3k_{nl} \cdot \alpha^2$ is larger than $T_0 \cdot cos(\theta - \alpha)$

When the magnitude of $3k_{nl} \cdot \alpha^2$ is larger than the magnitude of $T_0 \cdot \cos(\theta - \alpha)$ in (6), the resonant frequency curve resembles the shape of an $|\alpha|$ curve. The $|\alpha|$ curve is symmetric with respect to $\theta = 180^\circ$ and has two peaks at 90° and 270°. The $|\alpha|$ curve is also symmetric with respect to $\theta = 90^\circ$ and $\theta = 270^\circ$ in the range of 0°–180° and 180°–360°, respectively. This is the case when the external magnetic fields are 0.975 and 1.95 mT for all three beam widths (w_b = 10, 20, and 30 μm) and when the beam width is 10 μm at the external magnetic field of 50 μT, as shown in table 2. The numerical values of $3k_{nl} \cdot \alpha^2$ and $T_0 \cdot \cos(\theta - \alpha)$ are plotted in figures 5(*a*), (*c*) and (*e*) for the beam widths of 10, 20, and 30 μm, respectively. This shows that the magnitude of $3k_{nl} \cdot \alpha^2$ is larger than the magnitude of $T_0 \cdot \cos(\theta - \alpha)$ and this magnitude difference becomes large as the beam width decreases. Even though the nonlinear stiffness coefficient (k_{nl}) decreases as the beam width decreases (table 2), the product of k_{nl} and α^2 increases because α^2 increases at a faster rate, as shown in figure 6. Accordingly, the resonant frequency curves resemble the shape of $|\alpha|$ (figures 5(*b*), (*d*) and (*f*)) and the normalized sensitivity increases as the beam width

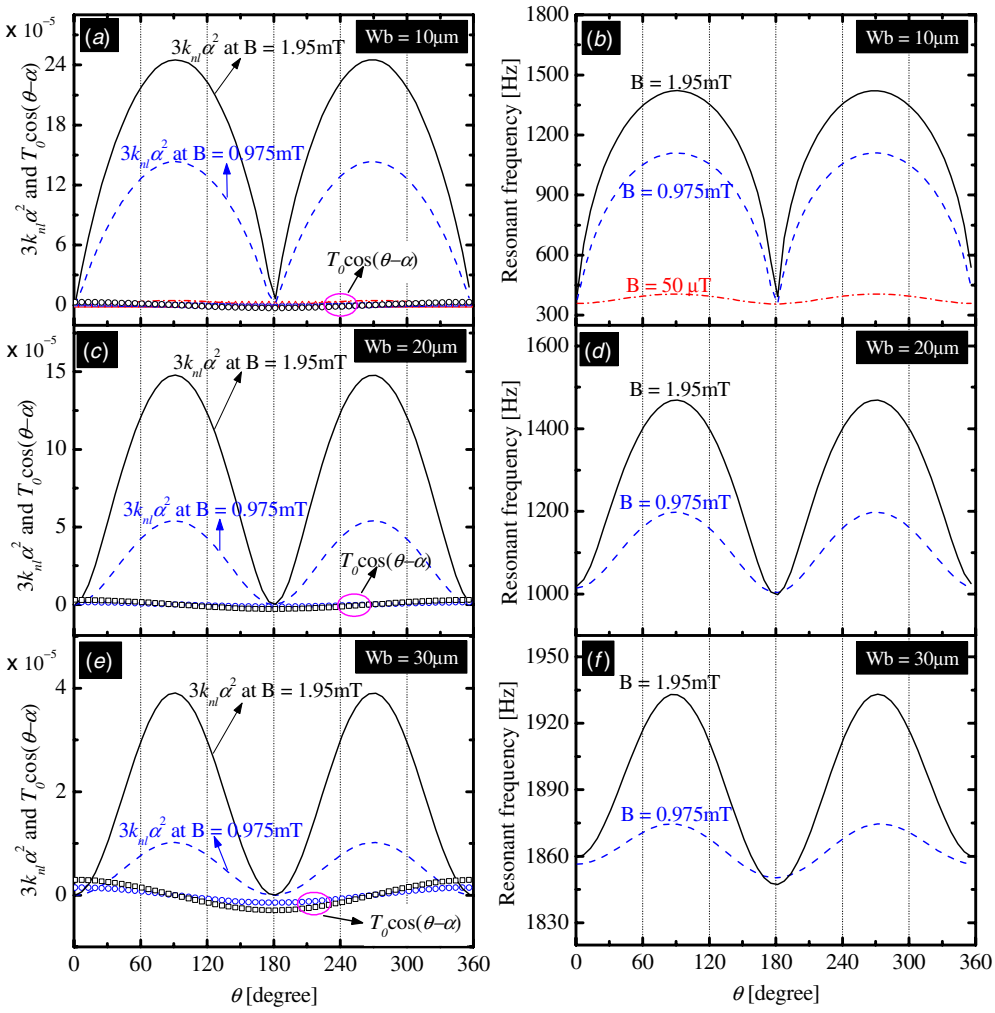

Figure 5. Comparison of $3k_{\mathrm{nl}} \cdot \alpha^2$ and $T_0 \cdot \cos(\theta - \alpha)$ for the beam widths of (*a*) 10, (*c*) 20, and (*e*) 30 μm and the resonant frequency curves for the beam widths of (*b*) 10, (*d*) 20, and (*f*) 30 μm at various external magnetic fields.

Table 2. Effects of the beam width on sensitivity. The difference between the maximum and minimum resonant frequencies divided by the minimum resonant frequency between $\theta = 0^\circ$ and 90° is taken as a measure of sensor performance. Also refer to figures 5, 7 and 8.

				$\Delta f_c/(f_c$ degree) (mHz (Hz degree)$^{-1}$)		
Beam width (μm)	k_{l} (10^{-6} N m)	k_{nl} (10^{-3} N m)	Resonant frequency at $\theta = 0^\circ$ (Hz)	50 μT	0.975 mT	1.95 mT
10	16.56	91.2	358.3	1.5	21.5	27.8
20	132.13	187	1009.4	0.0112	2.0	4.88
30	445.48	316	1853.5	0.000 94	0.11	0.44

decreases. The normalized sensitivity also increases as the external magnetic field increases because of the higher torque, which causes $f_{\max}$ to increase at a given beam width (table 2).

2.2. *Case 2: $3k_{\mathrm{nl}} \cdot \alpha^2$ is comparable to $T_0 \cdot cos(\theta - \alpha)$*

This is the case when the beam width is 20 μm and the external magnetic field is 50 μT, as shown in table 2. The magnitudes of $3k_{\mathrm{nl}} \cdot \alpha^2$ and $T_0 \cdot \cos(\theta - \alpha)$ are in the same order as shown in figure 7(*a*). The resonant frequency curve is similar to case 1 except that the resonant frequency at $\theta = 180^\circ$ is much lower than when $\theta = 0^\circ$ since the magnitude of the $T_0 \cdot \cos(\theta - \alpha)$ is minimal at $\theta = 180^\circ$ (figure 7(*b*)).

2.3. *Case 3: $3k_{\mathrm{nl}} \cdot \alpha^2$ is smaller than $T_0 \cdot cos(\theta - \alpha)$*

This is the case when the beam width is 30 μm at the external magnetic field of 50 μT, as shown in table 2. Figure 8(*a*) shows that $T_0 \cdot \cos(\theta - \alpha)$ is larger than $3k_{\mathrm{nl}} \cdot \alpha^2$ in magnitude. Accordingly, the resonant frequency curve is mainly determined by $T_0 \cdot \cos(\theta - \alpha)$, as shown in figure 8(*b*). For the previous cases, the highest resonant frequency occurs at $\theta = 90^\circ$ and 270°. However, for this case, the highest

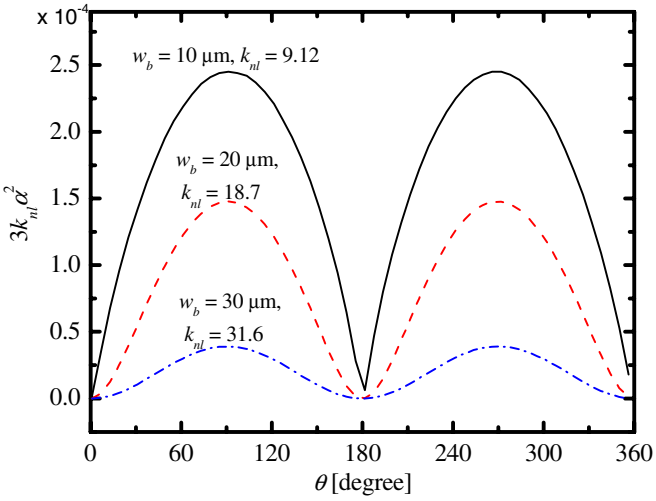

Figure 6. $3k_{\mathrm{nl}} \cdot \alpha^2$ as a function of θ for the 10, 20, and 30 μm beam widths at the external magnetic field of 1.95 mT. Note that k_{nl} increases while $k_{\mathrm{nl}} \cdot \alpha^2$ decreases as the beam width increases.

resonant frequency occurs at $\theta = 0^\circ$ $(= 360^\circ)$ due to the larger magnitude of $T_0 \cdot \cos(\theta - \alpha)$ than $3k_{\mathrm{nl}} \cdot \alpha^2$. The normalized sensitivity, calculated between $\theta = 0^\circ$ and 180°, is very small compared to the first two cases. This implies that in order to maximize the sensitivity, $3k_{\mathrm{nl}} \cdot \alpha^2$ has to be larger than $T_0 \cdot \cos(\theta - \alpha)$ at a given torque T_0.

3. Enhancing sensing performance by exploiting nonlinear effects

In the previous sections, the sensing performance is characterized by varying the beam width while other parameters are held constant. Based on the discussions in cases 1, 2, and 3, higher sensing performance can be achieved when the magnitude of $k_{\mathrm{nl}} \cdot \alpha^2$ is greater than that of $T_0 \cdot \cos(\theta - \alpha)$. This can be achieved by lowering the torsional linear stiffness, k_{l}, thereby increasing the deviation angle, α, at a given torque. Although k_{nl} decreases as the beam width decreases, the product of k_{nl} and α^2 increases since α^2 increases at a faster rate. Minimization of k_{l} can be achieved by either increasing the length of the beam or reducing the width of the beam. In both cases, the mechanical resonator becomes more susceptible to shocks and vibrations and can easily be broken.

Sensing performance can also be improved by maximizing the nonlinear stiffness coefficient (k_{nl}), as was discussed before. For example, when the linear stiffness is determined, the sensitivity is maximized by increasing the nonlinearity [10]. One way of increasing k_{nl} while keeping k_{l} constant is to design the mechanical resonator with thinner beams while increasing the number of beams. Thinner beams make k_{l} smaller; however, this is compensated with more beams, which bring the linear stiffness (k_{l}) of the resonator back to its original value in order to maintain mechanical stability. Furthermore, nonlinearity increases as well because the ratio of deflection to beam width increases. In other words, even at the same amount of deflection, each beam undergoes more stress since the deflection with respect to its width increases, thereby increasing the nonlinearity of the system [14].

To illustrate this, three different resonator geometries are chosen, as shown in figure 9, and analyzed, where the numbers of beams and the widths of beams are simultaneously adjusted such that their linear stiffness coefficients are the same. The selected numbers of beams are 4, 8, and 16 and their widths are 20, 15.9, and 12.6 μm, respectively.

The deflection versus force curves are plotted for these resonators in the inset of figure 10. The structure with 16 beams exhibits the highest nonlinearity followed by eight-beam and four-beam structures in that order. The lateral linear stiffness coefficients ($k_{\delta,1}$) are found to be 33, 16.5, and 8.3 N m^{-1} for 4, 8, and 16 beams, respectively. Note that $k_{\delta,1}$ in figure 10 is obtained from a single beam. Therefore, the overall $k_{\delta,1}$ of the resonator is calculated by multiplying it with the number of beams. The lateral nonlinear stiffness coefficients ($k_{\delta,\mathrm{nl}}$) are found to be 4.7×10^{10}, 3.6×10^{10}, and 2.9×10^{10} N m for 4, 8, and 16 beams, respectively. Hence, by using (11), the torsional linear stiffness coefficients (k_{l}) are calculated to be 132.13, 132.28, and 132.47 μN m for 4, 8, and 16 beams, respectively, and the torsional nonlinear stiffness coefficients (k_{nl}) are calculated to be 187, 291, and 462 mN m for 4, 8, and 16 beams, respectively. Table 3 summarizes the simulation results, including resonator dimension.

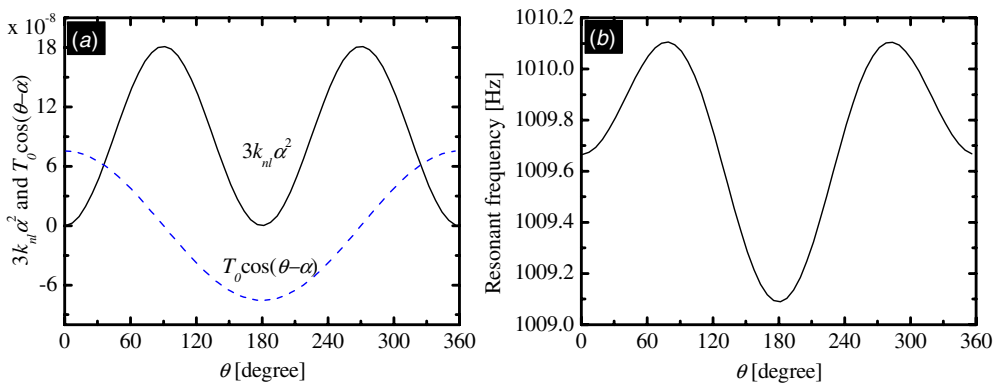

Figure 7. (*a*) Comparison of $3k_{\mathrm{nl}}\alpha^2$ and $T_0 \cdot \cos(\theta - \alpha)$ for the beam width of 20 μm at the external magnetic field of 50 μT. Note that $3k_{\mathrm{nl}}\alpha^2$ is comparable to $T_0 \cdot \cos(\theta - \alpha)$ in magnitude. (*b*) Resonant frequency as a function of θ.

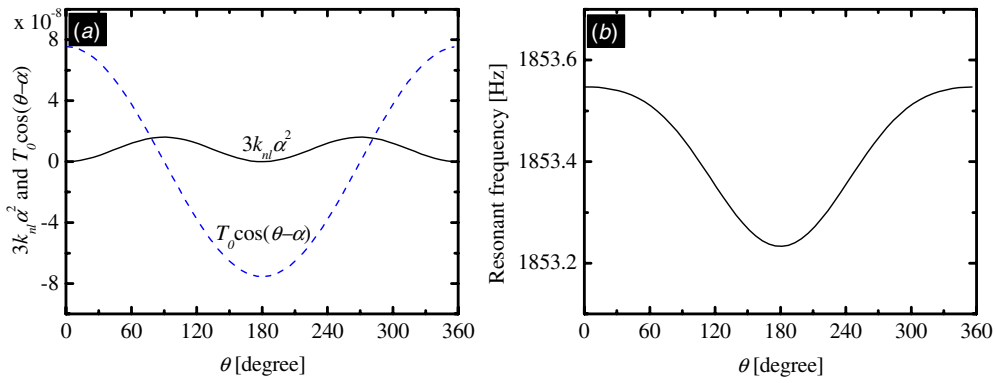

Figure 8. (*a*) Comparison of $3k_{\mathrm{nl}}\alpha^2$ and $T_0 \cdot \cos(\theta - \alpha)$ for the beam width of 30 μm at the external magnetic field of 50 μT. Note that $T_0 \cdot \cos(\theta - \alpha)$ is larger than $3k_{\mathrm{nl}}\alpha^2$ in magnitude. (*b*) Resonant frequency as a function of θ.

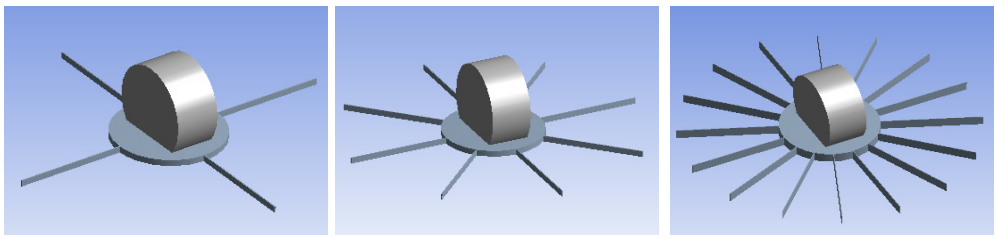

(*a*) (*b*) (*c*)

Figure 9. Three different resonator geometries with (*a*) 4 beams ($w_b = 20$ μm), (*b*) 8 beams ($w_b = 15.9$ μm), and (*c*) 16 beams ($w_b = 12.6$ μm).

Table 3. Effects of resonator geometries (beam width and number of beams) on sensitivity. The difference between the maximum and minimum resonant frequencies divided by the minimum resonant frequency between $\theta = 0^\circ$ and 90° is taken as a measure of sensor performance.

Number of beams	Beam width (μm)	k_{l} (10^{-6} N m)	k_{nl} (10^{-3} N m)	Resonant frequency at $\theta = 0^\circ$, f_c (Hz)	Sensitivity $\Delta f_c/(f_c \cdot \text{degree})$ (mHz (Hz degree)$^{-1}$)		
					50 μT	0.975 mT	1.95 mT
4	20	132.13	187	1009.38	0.0112	2.001	4.879
8	15.9	132.28	291	1009.95	0.0153	2.756	6.157
16	12.6	132.47	462	1010.68	0.022	3.727	7.659

As shown in table 3, the torsional linear stiffness coefficients, k_{l}, are set to be very close for the three designs by adjusting the beam width and the number of beams simultaneously. The four-beam resonator with a 20 μm beam width shows slightly lower k_{l} than the other two designs. As a result, the resonant frequency of the four-beam resonator is lowest among them. However, the torsional nonlinear stiffness coefficient, k_{nl}, increases as more beams are used. It is worthwhile mentioning that the narrower beam widths are used as more beams are added in order to increase the nonlinearity of a resonator while keeping its linear stiffness unchanged. Deviation angles are calculated using (3) and shown in figure 11(*a*). The deviation angle (α) becomes large as fewer beams are used where beam widths are simultaneously increased. Although the magnitude of α decreases as k_{nl} increases at a given θ, the product of k_{nl} and α^2 becomes large as k_{nl} increases at a given θ since k_{nl} increases at a faster rate, as shown in figure 11(*b*). The resonant frequencies are evaluated at 50 μT, 0.975 mT, and 1.95 mT for the three structures (figures 12(*a*) and (*b*)). In all cases, the higher the k_{nl}, the higher the sensitivity (table 3). Therefore, the concept of increasing the sensitivity by increasing the nonlinear stiffness coefficient at a given linear stiffness is demonstrated.

4. Silicon resonator fabrication and measurement

A test device to exploit the preceding phenomenon, a MEMS-based magnetic compass, was designed and fabricated. Fabrication includes two major processes: (1) fabrication of the mechanical resonator using inductively coupled plasma (ICP) silicon etching; and (2) assembly of the permanent magnet. The mechanical resonator fabrication is based

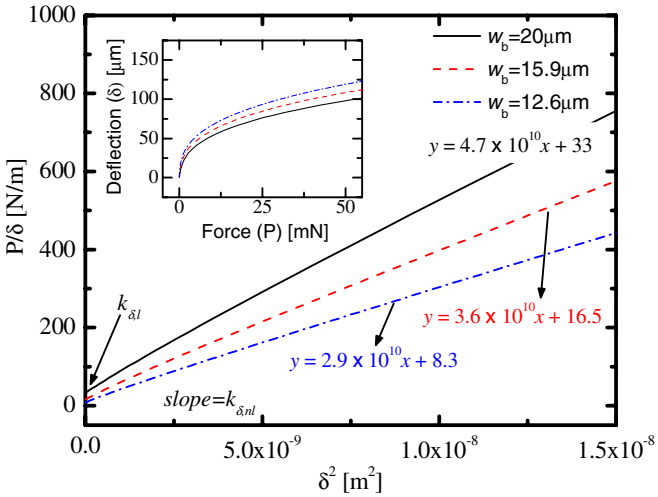

Figure 10. A nonlinear deflection of a single beam where one end is clamped and the other end is guided. The lateral nonlinear stiffness coefficient ($k_{\delta,\mathrm{nl}}$) corresponds to the slope and the lateral linear stiffness coefficient ($k_{\delta,1}$) is found at the intercept $\delta^2 = 0$. The inset shows the nonlinear dependence of the deflection on the applied force. The torsional linear (k_1) and nonlinear (k_{nl}) stiffness coefficients are calculated by (11).

on a two-mask, single-wafer silicon bulk micromachining process. A bottom recess is created by etching the bottom side of a silicon wafer to achieve a preferred beam thickness (figure 13(*a*)). Then, the top-side silicon wafer is etched to form a movable resonant disk, a recess for a permanent magnet, and support beams (figures 13(*a*) and (*b*)). ICP etching (Plasma-Therm ICP) is used for these silicon etching processes. Figure 13(*b*) shows a scanning electron microscopy (SEM) image of the fabricated device, which has eight beams with a beam width of 13.1 μm, a beam length of 2 mm, and a beam thickness of 110 μm. The neodymium–iron–boron (NdFeB) permanent magnet is adhered to the center of the resonator disk (figure 13(*c*)). Excitation and detection coils are hand wound on plastic tubes with a diameter of 1.5 mm and hybrid-assembled with the sensor (figure 13(*d*)). The number of turns is 300 for both the excitation and detection coils. The excitation and detection coils are placed in the same plane, thereby maximizing the magnetic flux linkage between the permanent magnet and the detection coil. The crosstalk between the two coils is negligible in the positive closed loop configuration.

The resonator is embedded within a positive feedback loop to form a self-resonant oscillator system (figure 14) [38]. In this configuration, the resonator is forced to oscillate at its resonant frequency without an externally applied driving signal. This type of configuration is useful in resonant sensing applications if the resonance frequency is the output signal of interest, and will be used to determine the sensitivity of the resonant sensor to magnetic field.

The excitation coil generates a time-varying magnetic field around the permanent magnet. The resonator oscillates if the natural frequency of the resonator is matched with the frequency of the time-varying magnetic field generated by the excitation coil. Accordingly, the permanent magnet adhered to the oscillating resonator also generates a time-varying magnetic field. The mechanical resonator works as a frequency-determining element in a self-oscillating amplifying feedback loop. The detection coil induces a voltage from this time-varying magnetic field generated by the oscillating permanent magnet. The output of the detection coil is connected to the input of the positive closed-loop circuit which consists of an amplifier, a phase shifter, and a Schmitt trigger. The output signal of the detection coil is amplified with the amplifier and then passed through the phase shifter and the Schmitt trigger. The phase shifter adjusts the phase of the closed loop such that the output signal of the detection coil is fed into the excitation coil in phase to form a positive feedback. The condition for a positive feedback is that a portion of the output is combined in phase with the input. The Schmitt trigger improves noise immunity and thus limits the peak-to-peak magnitude of the excitation signal to prevent large oscillation of the resonator. A frequency counter is connected at the end of the circuitry to read the resonant frequency of the resonator. An external magnetic field is applied through two Helmholtz coils.

The excitation coil utilized 1.4 mVrms with a total power consumption of 0.24 μW. The remaining circuitry, excluding

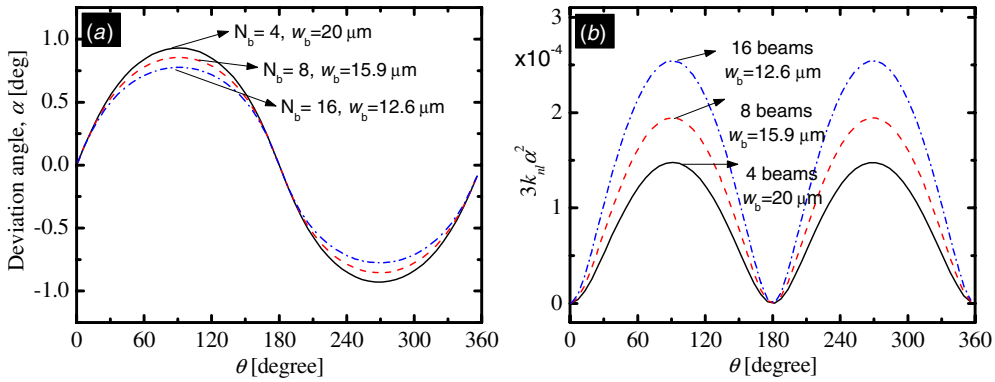

Figure 11. Deviation angles (α) and $3k_{\mathrm{nl}} \cdot \alpha^2$ for 4-, 8-, and 16-beam structures simulated at an external magnetic field of 1.95 mT. (*a*) Deviation angle (α) as a function of θ. (*b*) Magnitude of $3k_{\mathrm{nl}} \cdot \alpha^2$ as a function of θ.

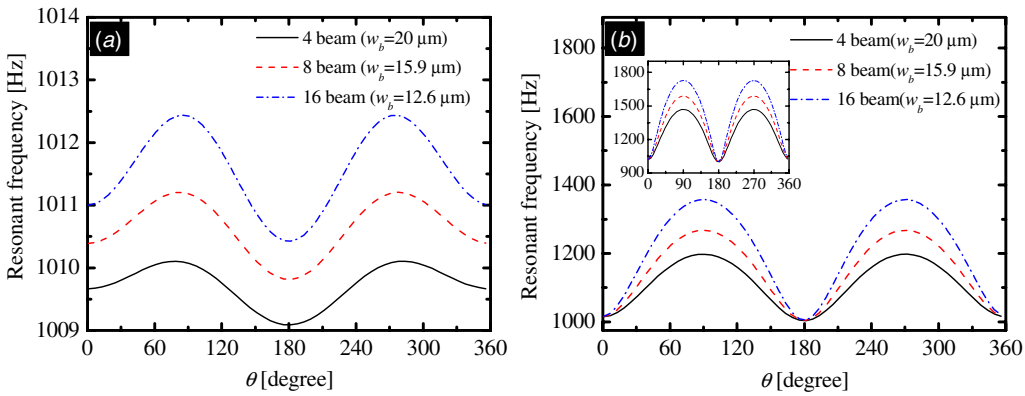

Figure 12. Simulated resonant frequencies for three different designs; 4 beams ($w_b = 20\ \mu$m), 8 beams ($w_b = 15.9\ \mu$m), and 16 beams ($w_b = 12.6\ \mu$m). (*a*) $B = 50\ \mu$T, (*b*) $B = 0.975$ mT, and (inset) $B = 1.95$ mT.

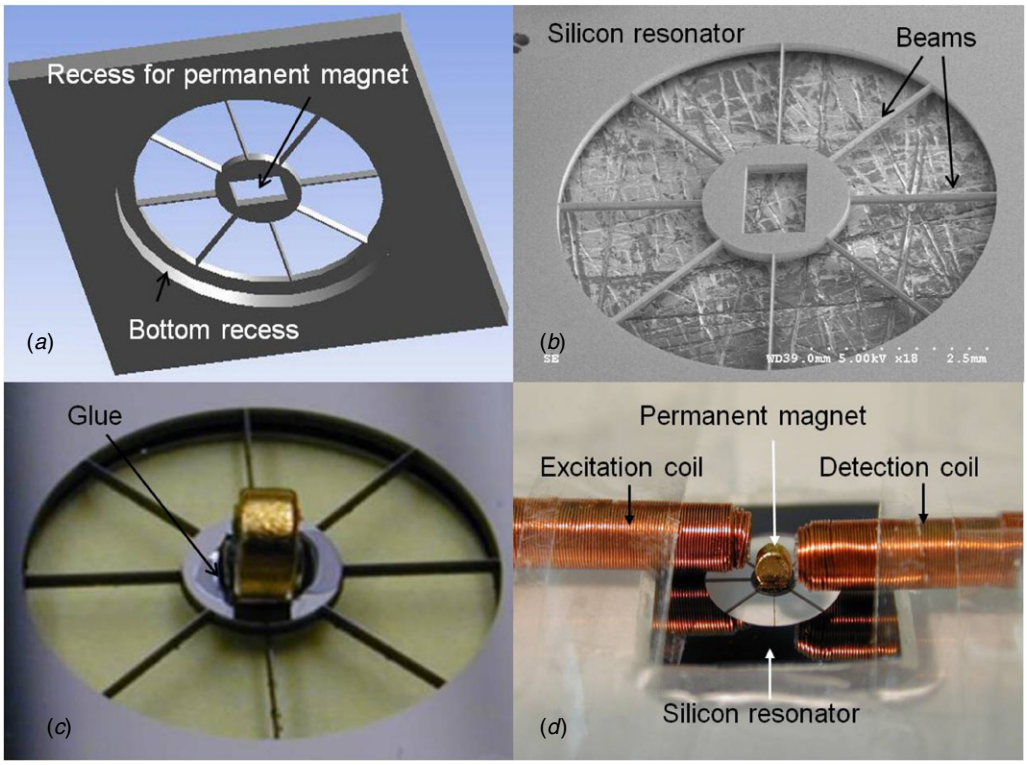

Figure 13. Silicon resonator fabrication: (*a*) ICP etching bottom and top silicon surface, (*b*) SEM image of resonator with eight beams, (*c*) permanent magnet assembly, and (*d*) assembly of excitation and sensing coils.

the frequency counter, utilized low power op-amps from Analog Devices (OP 490) with a power consumption of 138 μW. The total power consumption was therefore less than 140 μW.

5. Results

Three mechanical resonators with different beam widths and numbers of beams were fabricated and tested at various external magnetic fields (figure 15); the number of beams was 3, 4, and 6 with 18.5, 14.6, and 13.1 μm beam widths, respectively. The beam widths were measured by SEM. The number of beams for the six-beam resonator was originally designed to be 8, but two of them were broken during the measurement (figure 15(*c*)). The broken beams were completely removed by using a laser.

The devices were tested at three different external magnetic fields: the Earth's magnetic field (50 μT), 0.195 mT, and 0.39 mT. The results are shown in figure 16. For the three-beam and four-beam structures, the resonant frequency curve is not exactly symmetric with respect to $\theta = 180^\circ$. This is because either all of the beams in the resonator did not have

Table 4. Comparison of the normalized sensitivity (mHz (Hz degree)$^{-1}$). The resonant frequency is taken from the curve of the Earth's magnetic field (50 μT) measurement at $\theta = 0^\circ$.

				Normalized sensitivity (mHz (Hz degree)$^{-1}$) and (sensing resolution averaged over $\theta = 0^\circ$–90° (Hz/degree))		
N_b	w_b (μm)	Calculated k_1 (10^{-4} N m)	Resonant frequency (Hz) at $\theta = 0^\circ$	Earth's field	0.195 mT	0.39 mT
3	18.5	4.07	1881	0.009 (0.016)	0.017 (0.032)	0.036 (0.068)
4	14.6	1.80	1248.25	0.086 (0.107)	0.192 (0.239)	0.431 (0.538)
6	13.1	2.36	1437.45	0.196 (0.282)	0.509 (0.732)	0.876 (1.26)

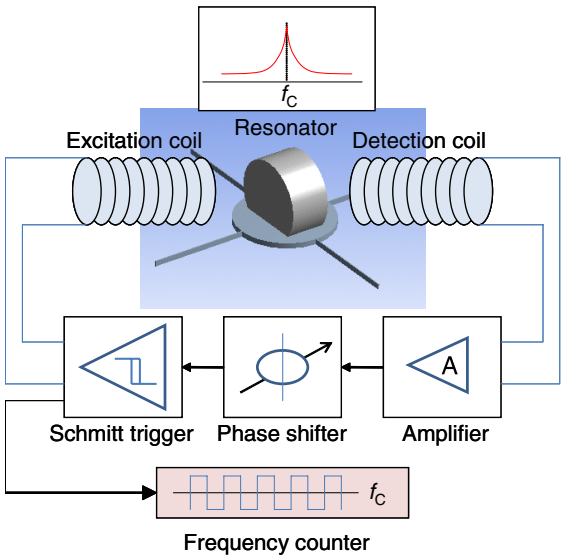

Figure 14. Complete magnetic sensing system. The fabricated mechanical resonator is embedded within a positive feedback loop that tracks the changes in the resonant frequency. The resonator is electromagnetically excited and detected by coils.

the identical width or the permanent magnet was not placed in exactly the center of the resonator disk, or both. Table 4 summarizes the measurement results. A sensing resolution averaged over $\theta = 0^\circ$–90° in terms of the resonant frequency change per unit rotational degree is provided in parentheses in sensitivity columns in table 4. The changes in the resonant frequency, $df_c/d\theta$, are not uniform throughout the rotational angle (from $\theta = 0^\circ$ to $\theta = 360^\circ$), i.e. minimal change at $\theta = 0^\circ$, 90°, 180°, and 270° and maximal change at $\theta = 45^\circ$, 135°, 225°, and 315°.

k_1 is calculated using (8) and is given by $k_1 = (2\pi f_c)^2 I - T_0$ at $\theta = 0^\circ$. A mass moment of inertia (I) was obtained by FEM simulation; $I = 2.92 \times 10^{-12}$, 2.93×10^{-12}, and 2.90×10^{-12} kg m^2 for the three-beam, four-beam, and six-beam structures, respectively. Since the resonant frequencies in table 4 are obtained from the curves of the Earth's magnetic field measurement at $\theta = 0^\circ$ shown in figure 16, T_0 at 50 μT, 7.6×10^{-8} N m, is used to calculate k_1. The torsional linear stiffnesses of the four-beam and six-beam resonators are 44% and 58% of that of the three-beam resonator, respectively. This lower linear stiffness results in better sensing performance for the resonators with four beams and six beams than the resonator with three beams at all magnetic fields.

For the resonator with six beams, a sensitivity of 0.282 Hz/degree is obtained for the Earth's magnetic field, and 0.732 and 1.260 Hz/degree are achieved for the applied fields of 0.195 and 0.39 mT, respectively (table 4). Although the resonator with six beams has higher linear stiffness than the resonator with four beams, it shows higher sensing performances at all measured external magnetic fields and this improvement can be attributed to the higher nonlinearity in the six-beam resonator due to its narrow beam width compared to the four-beam resonator. As configured, the single resonator response is symmetric in θ; therefore, compass orientations with opposite directions cannot be directly resolved. This limitation can be overcome by various means, including the use of multiple resonators on a single chip.

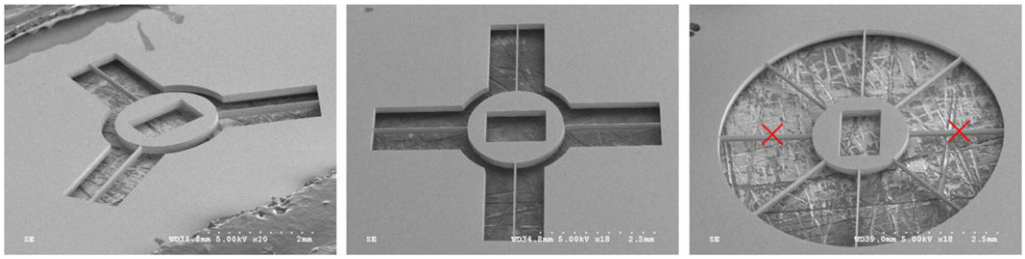

(*a*) (*b*) (*c*)

Figure 15. Micromachined silicon resonators. (*a*) Three-beam structure with 18.5 μm in beam width, (*b*) four-beam structure with 14.6 μm in beam width, and (*c*) six-beam structure with 13.1 μm in beam width.

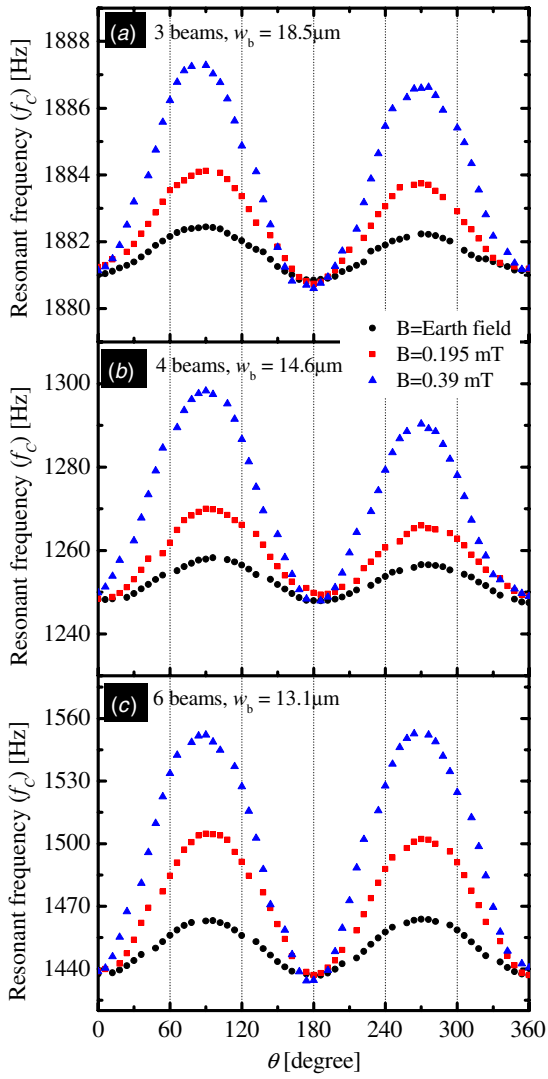

Figure 16. Resonant frequency measurement as a function of the rotational angle, θ: (*a*) three beams with $w_b = 18.5$ μm, (*b*) four beams with $w_b = 14.6$ μm, and (*c*) six beam with $w_b = 13.1$ μm. The devices were tested at the Earth's magnetic field, 0.195 and 0.39 mT.

6. Conclusion

It has been demonstrated that nonlinear effects in resonating structures can be used to increase the sensitivity of sensors based on these structures. These effects are illustrated with a model that consists of a disk-type resonator supported by multiple beams. The effects of nonlinearity on sensitivity have been characterized as a function of beam width and the number of beams using an analytical model. By increasing the number of beams while reducing beam width (and thereby maintaining constant nominal linear resonant frequency), large nonlinearity has been obtained, resulting in increased sensitivity. In order to demonstrate these effects, torsional resonant magnetic sensors have been designed, fabricated, and characterized to measure the direction of the Earth's magnetic field. The micromachined resonators have three, four, and six beams with beam widths of 18.5, 14.6, and 13.1 μm, respectively. The torsional linear stiffnesses of the four-beam and six-beam resonators were 44% and 58% of that of the three-beam resonator, thereby exhibiting higher sensing performance than the three-beam resonator. Although the linear stiffness coefficient of the six-beam resonator was larger than that of the four-beam resonator, the six-beam resonator showed higher normalized sensitivities at all of the measured external magnetic fields due to the large nonlinear stiffness, demonstrating the beneficial effects of nonlinear maximization.

A total system power consumption of less than 140 μW including a resonator actuation voltage of 1.4 mVrms has been demonstrated with a sensitivity of 0.28 Hz/degree to the Earth's magnetic field. It can be operated continuously for more than 3000 h with a standard button cell (CR2025; 3 V, 140 mAh). Such a low power consumption level enables continuous magnetic field sensing for portable electronics and potentially wristwatch-type personal navigation applications.

References

[1] Bahreyni B and Shafai C 2007 A resonant micromachined magnetic field sensor *IEEE Sensors J.* **7** 1326–34
[2] Baschirotto A, Borghetti F, Dallago E, Malcovati P, Marchesi M, Melissano E, Siciliano P and Venchi G 2006 Fluxgate magnetic sensor and front-end circuitry in an integrated microsystem *Sensors Actuators* A **132** 90–7
[3] Baschirotto A, Cabrini A, Dallago E, Malcovati P, Marchesi M and Venchi G 2006 Development and analysis of a PCB vector 2-D magnetic field sensor system for electronic compasses *IEEE Sensors J.* **6** 365–71
[4] Baschirotto A, Dallago E, Malcovati P, Marchesi M and Venchi G 2007 A fluxgate magnetic sensor: from PCB to micro-integrated technology *IEEE Trans. Instrum. Meas.* **56** 25–31
[5] Brand O and Baltes H 1998 Micromachined resonant sensors—an overview *Sensors Update* **4** 3–51
[6] Brugger S and Paul O 2008 Resonant magnetic microsensor with μT resolution *21st IEEE Int. Conf. on Micro Electro Mechanical Systems (2008), MEMS 2008* pp 944–7
[7] Brugger S and Paul O 2009 Field-concentrator-based resonant magnetic sensor with integrated planar coils *J. Microelectromech. Syst.* **18** 1432–43
[8] Caruso M J 2000 Applications of magnetic sensors for low cost compass systems *IEEE Position Location and Navigation Symp. (2000)* pp 177–84
[9] Choi S, Kim S-H, Yoon Y-K and Allen M G 2006 A magnetically excited and sensed MEMS-based resonant compass *IEEE Trans. Magn.* **42** 3506–8
[10] Choi S, Kim S-H, Yoon Y-K and Allen M G 2007 Exploitation of nonlinear effects for enhancement of the sensing performance of resonant sensors *Int. Solid-State Sensors, Actuators and Microsystems Conf. (2007), TRANSDUCERS 2007* pp 1745–8
[11] Choi W-Y, Hwang J-S and Choi S-O 2004 The microfluxgate magnetic sensor having closed magnetic path *IEEE Sensors J.* **4** 768–71
[12] Eyre B, Pister K S J and Kaiser W 1998 Resonant mechanical magnetic sensor in standard CMOS *IEEE Electron Device Lett.* **19** 496–8
[13] Fan J, Li X P and Ripka P 2006 Low power orthogonal fluxgate sensor with electroplated $Ni_{80}Fe_{20}$/Cu wire *J. Appl. Phys.* **99** 08B311
[14] Frisch-Fay R 1962 *Flexible Bars* (Washington: Butterworths)
[15] Herrera-May A L, Garcia-Ramirez P J, Aguilera-Cortes L A, Martinez-Castillo J, Sauceda-Carvajal A, Garcia-Gonzlez L and Figueras-Costa E 2009 A resonant magnetic field

microsensor with high quality factor at atmospheric pressure *J. Micromech. Microeng.* **19** 015016
[16] Hwang J S, Park H S, Shim D S, Na K W, Choi W Y and Choi S O 2003 Electronic compass using two-axis micro fluxgate sensing element *The 12th International Conference on Solid State Sensors, Actuators and Microsystems (Boston, 8–12 June 2003)* **2** 1618–21
[17] Judy J W, Yang H, Myung N, Irazoqui-Pastor P, Schwartz M, Nobe K and Yang K 2000 Ferromagnetic micromechanical magnetometers *Late News, Technical Digest of Solid-State Sensor and Actuator Workshop (Hilton Head Island)* pp 15–6
[18] Kacem N *et al* 2009 Nonlinear dynamics of nanomechanical beam resonators: improving the performance of NEMS-based sensors *Nanotechnology* **20** 275501
[19] Kádár Z, Bossche A, Sarro P M and Mollinger J R 1998 Magnetic-field measurements using an integrated resonant magnetic-field sensor *Sensors Actuators* A **70** 225–32
[20] Kozinsky I, Postma H W C, Bargatin I and Roukes M L 2006 Tuning nonlinearity, dynamic range, and frequency of nanomechanical resonators *Appl. Phys. Lett.* **88** 253101
[21] Kyynäräinen J *et al* 2008 A 3D micromechanical compass *Sensors Actuators* A **142** 561–8
[22] Leichle T C, Von Arx M, Reiman S, Zana I, Wenjing Y and Allen M G 2004 A low-power resonant micromachined compass *J. Micromech. Microeng.* **14** 462–70
[23] Lenz J and Edelstein S 2006 Magnetic sensors and their applications *IEEE Sensors J.* **6** 631–49
[24] Lenz J E 1990 A review of magnetic sensors *Proc. IEEE* **78** 973–89
[25] Liakopoulos T M and Ahn C H 1999 A micro-fluxgate magnetic sensor using micromachined planar solenoid coils *Sensors Actuators* A **77** 66–72
[26] Marchesi M, Baschirotto A, Borghetti F, Dallago E, Malcovati P, Melissano E, Siciliano P and Venchi G 2006 Fluxgate magnetic sensor and front-end circuitry in an integrated microsystem *Sensors Actuators* A **132** 90–7
[27] Montaigne F, Schuhl A, Van Dau F N and Encinas A 2000 Development of magnetoresistive sensors based on planar Hall effect for applications to microcompass *Sensors Actuators* A **81** 324–7
[28] Na K-W, Yuan J, Ji J-H and Choi S-O 2006 Microfluxgate sensor with amorphous cobalt (Co–Nb–Zr) soft magnetic core for electronic compass *J. Appl. Phys.* **99** 08M306
[29] Park H-S, Hwang J-S, Choi W-Y, Shim D-S, Na K-W and Choi S-O 2004 Development of micro-fluxgate sensors with electroplated magnetic cores for electronic compass *Sensors Actuators* A **114** 224–9
[30] Platif A, Kubik J, Vopalensky M and Ripka P 2003 Precise AMR magnetometer for compass *Proc. IEEE Sensors (2003)* vol 1 pp 472–6
[31] Popovic R S, Drljaca P M and Schott C 2002 Bridging the gap between AMR, GMR, and Hall magnetic sensors *23rd Int. Conf. on Microelectronics (2002), MIEL 2002* vol 1 pp 55–8
[32] Racz R, Schott C and Huber S 2004 Electronic compass sensor *Proc. IEEE Sensors (2004)* vol 3 pp 1446–9
[33] Ripka P 1992 Review of fluxgate sensors *Sensors Actuators* A **33** 129–41
[34] Ripka P 2000 New directions in fluxgate sensors *J. Magn. Magn. Mater.* **215–216** 735–9
[35] Ripka P 2003 Advances in fluxgate sensors *Sensors Actuators* A **106** 8–14
[36] Ripka P and Janosek M 2010 Advances in magnetic field sensors *IEEE Sensors J.* **10** 1108–16
[37] Robbes D 2006 Highly sensitive magnetometers—a review *Sensors Actuators* A **129** 86–93
[38] Sunier R, Vancura T, Li Y, Kirstein K U, Baltes H and Brand O 2006 Resonant magnetic field sensor with frequency output *J. Microelectromech. Syst.* **15** 1098–107
[39] Van Der Meer J, Makinwa K and Huijsing J 2007 Standard CMOS Hall-sensor with integrated interface electronics for a 3D compass sensor *Proc. IEEE Sensors (2007)* pp 1101–4
[40] Vcelak J, Ripka P, Kubik J, Platil A and Kaspar P 2005 AMR navigation systems and methods of their calibration *Sensors Actuators* A **123–124** 122–8
[41] Yang H H, Myung N V, Yee J, Park D Y, Yoo B Y, Schwartz M, Nobe K and Judy J W 2002 Ferromagnetic micromechanical magnetometer *Sensors Actuators* A **97–98** 88–97